INSTITUTE OF PHYSICS PUBLISHING JOURNAL OF PHYSICS G: NUCLEAR AND PARTICLE PHYSICS

J. Phys. G: Nucl. Part. Phys. **27** (2001) 2051–2064 PII: S0954-3899(01)24272-8

In-flight performance of SilEye-2 experiment and cosmic ray abundances inside the Mir space station

V Bidoli[1], M Casolino[1,10], E De Grandis[1], M P De Pascale[1], G Furano[1], A Morselli[1], L Narici[1], P Picozza[1], E Reali[1], R Sparvoli[1], A Galper[2], A Khodarovich[2], M Korotkov[2], A Popov[2], N Vavilov[2], G Mazzenga[3], M Ricci[3], G Castellini[4], S Avdeev[5], M Boezio[6], W Bonvicini[6], A Vacchi[6], N Zampa[6], P Papini[7], P Spillantini[7], P Carlson[8] and C Fuglesang[9]

[1] INFN ROMA2 and University of Roma Tor Vergata, Italy
[2] Moscow Engineering and Physics Institute, Moscow, Russia
[3] LNF, INFN, Frascati, Rome, Italy
[4] IROE of CNR, Florence, Italy
[5] Russian Space Corporation 'Energia', Korolev, Moscow Region, Russia
[6] University of Trieste and INFN Sezione Trieste, Italy
[7] University of Firenze and INFN Sezione Firenze, Italy
[8] Royal Institute of Technology, Stockholm, Sweden
[9] European Astronaut Centre, ESA, Cologne, Germany

E-mail: casolino@roma2.infn.it

Received 24 April 2001, in final form 9 July 2001
Published 13 September 2001
Online at stacks.iop.org/JPhysG/27/2051

Abstract

Cosmic ray measurements performed with the instrument SilEye-2 on the Mir space station are presented. SilEye-2 is a silicon detector telescope used to study the causes of the light flashes perceived by astronauts. As a stand-alone device, it monitors the short- and long-term radiation composition inside Mir. The cosmic ray detector consists of an array of six active silicon strip detectors which allow nuclear identification of cosmic rays up to iron. The device was operational for more than 1000 h in the years 1998–2000, also measuring several solar particle events. In this work we present the in-flight performance of the instrument and nuclear abundance data from boron to silicon above $\simeq$150 MeV n^{-1} inside Mir.

1. Introduction

A detailed study and understanding of the radiation environment in space and its effects on human physiology has increasing importance in light of work on the International Space Station (ISS) and of a future mission to Mars. Radiation in orbit comes from cosmic rays of different energies and origins. In addition to the galactic component, which is modulated by the

[10] Author to whom correspondence should be addressed.

solar activity at low energies, there are also solar energetic particles associated with transient phenomena such as solar flares and coronal mass ejections. Inside Earth's magnetosphere there is also a significant contribution from trapped particles: for the well known proton and electron belts, recent studies have shown a more complex nuclear composition, for instance, with trapped components of anomalous cosmic rays [1]. For low Earth orbits such as those of Mir, ISS or the Shuttle (altitude of 300–400 km, inclination of 51.6°) the effect of trapped radiation is most evident in the South Atlantic Anomaly (SAA). This is a region located between South America and Africa where the geomagnetic field is lower and the particle flux increases. It is also important to study the $Z > 1$ cosmic ray component for its high quality factor, which, even with a low flux, can give a non-negligible contribution to the dose absorbed by astronauts.

In addition to the effects of radiation, there are also other processes that need to be studied in order to gain a more complete knowledge of the human response to the space environment. One of these phenomena is the 'light flashes' (LF) effect, originally predicted in [2, 3] and reported for the first time in 1969 by the Apollo-11 mission to the Moon. Subsequently, LF were observed by astronauts in the Apollo, Skylab, Shuttle and Mir missions [4, 5, 7]. The SilEye-1 and 2 experiments were designed to study this phenomenon and the radiation environment on board the Mir space station. In order to correlate LF observations by the cosmonaut with cosmic rays it is necessary to measure charge, energy deposition and direction of the incoming particles in real time. The use of active silicon detectors [8, 9] is necessary to meet these requirements with the limitations of mass, size and power consumption. SilEye-1 was operational on Mir between December 1995 and December 1997 [10, 11]. It performed the first LF observations on Mir and carried the prototype of the silicon detector. SilEye-2 [12, 13] was first turned on in August 1998 with systematic observations starting in October 1998. It was operational in various periods until 28 August 1999. When the last crew reached Mir in March 2000, SilEye-2 was used again during the mission (until June 2000).

In this work we discuss the in-flight performance of the detector and particle composition on board the Mir space station using data gathered between August 1998 and August 1999. This data set consists of 93 sessions, 17 of which were devoted to light flashes observation. More than 10^7 particle events have been acquired in 1068 h of observation time: during these observations seven solar particle events (SPEs) were also detected. The latest data set (year 2000) is currently under analysis. LF results are presented in [14].

2. The experimental device

SilEye-2 consists of a silicon detector telescope, shown in figure 1, housed in an aluminium box, coupled to a 'helmet' with an eye mask, and worn by the cosmonaut. The device is connected to a laptop computer equipped with a data acquisition card and a joystick. The detector is small (maximum dimension 26.4 cm, mass 5.5 kg), robust and easy to handle. Computer-based control software performs data handling and storage. To carry out LF observations, the astronaut wears the helmet which holds the detector box and presses the joystick button when he observes LF. Data come, therefore, from two independent sources: the particle track recorded by the silicon detector and the observation of the LF by the astronaut. The helmet has a mask that shields the astronaut's eyes from light; three internal LEDs allow one to cross-check the correct position of the detector, verify the dark adaptation of the observer and to measure his reaction time to normalize measurements performed by different astronauts.

The device can also be operated as a stand-alone cosmic ray detector without the presence of the cosmonaut; in this acquisition mode monitoring of the environmental radiation inside Mir is performed. Each event (cosmic ray or LF observation) has a time stamp (50 ms precision)

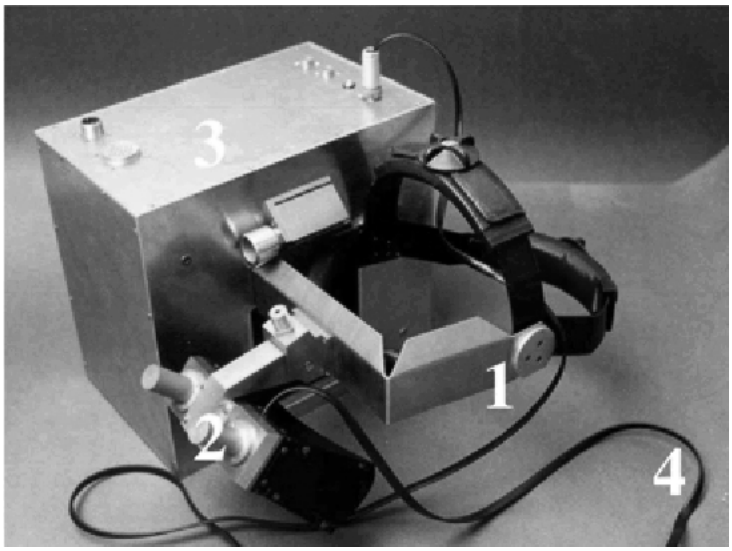

Figure 1. Photograph of the SilEye-2 helmet and detector case: 1, head mounting; 2, eye mask with internal LEDs; 3, detector box; 4, connection cable for the LEDs used for dark adaptation tests.

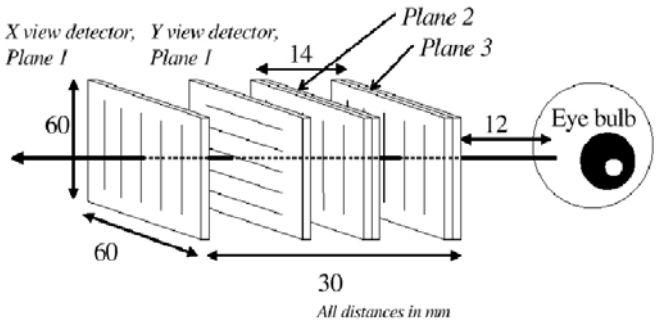

Figure 2. Schematic of the SilEye-2 silicon detector: six 16 strip silicon layers glued in pairs with strips aligned orthogonally form three planes (the two layers of the first plane are drawn separately). The position of the eye bulb is also shown.

to correlate it with the orbital position of Mir. A particle event is defined by the energetic and topological information coming from the strips hit by incoming particle(s); an LF event consists of the time of clicking the joystick button.

The particle detector telescope is made of a series of six silicon active wafer, originally developed in the construction of NINA-1 and 2 cosmic ray space telescopes [15,16]. The device structure is shown in figure 2. The detector is positioned on the temple of the cosmonaut in order to cover the maximum angle for cosmic rays impinging on the eye. In stand-alone mode for cosmic ray measurements it is placed in a specific location on Mir. The position of the device is recorded each session in order to reconstruct its orientation with respect to the station. Each of the six silicon wafers has an active area of 60×60 mm^2, divided into 16 strips 3.6 mm

Table 1. Left, threshold energy for absorption in 3 mm Al of the hull of Mir (E_{abs}); centre, threshold energy (after entrance in the Mir) for trigger (E_{min}); right, threshold energy for constant energy loss in the detector (E_{con}) (see text).

Z	E_{abs} (MeV n^{-1})	E_{min} (MeV n^{-1})	E_{con} (3 mm Al) (MeV n^{-1})
1 H	24	30	60
2 He	24	37	65
3 Li	28	40	75
4 Be	34	50	90
5 B	39	50	105
6 C	45	70	115
7 N	49	65	125
8 O	53	80	140
9 F	55	80	145
10 Ne	60	90	150
11 Na	61	95	155
12 Mg	66	100	165
14 Si	71	110	185
18 S	77	120	200
20 Ca	88	140	230
26 Fe	98	150	250

wide; the thickness is 380 ± 15 μm. Two wafers, glued orthogonally back to back, constitute a plane. Three planes are used together, for a total number of 96 strips and an active thickness of 2.28 mm. The distance between the silicon planes is 15 mm; the geometrical factor is 85 cm^2 sr if particles hitting the detector from both sides are considered. The silicon strips are depleted by a DC voltage of 36 V, supplied by batteries insulated from the rest of the circuit board. The outermost strips of plane 1 (1 and 16) are disconnected, while those of planes 2 and 3 are connected to the same readout channel. The readout channels saved in this way are used for housekeeping information. Among the housekeeping values are the inverse currents of each silicon plane. In addition, there are two analogue low rate meters (which measure the incident rate on plane 1, view X and Y, up to 400 Hz) and three analogue high rate meters (one per plane) which measure particle rates up to 20 kHz. We therefore have 88 physics and eight housekeeping channels for a total of 96 readouts per event.

Two passive absorbers (1 mm iron each) are inserted between the position-sensitive planes to extend the energy range. For single-track events, the particle trajectory is determined with an angular accuracy of 5°. Each analogue signal comes into the read-out board, which performs the tasks of analogue-to-digital conversion (ADC), trigger and calibration. For each trigger, data are converted by a 12 bit ADC and sent to FIFO (first in, first out) for acquisition by the read out card. The ADC has a dynamic range up to 12.2 pC of injected charge: thus SilEye-2 can measure particle energy losses per strip from 0.25 MeV (0.69 keV μm^{-1}) to about 300 MeV (830 keV μm^{-1}) and then determine the nuclear species. The analogic sum of the signals from the strips of each view is used as an input for the trigger system, performed by a PAL (programmable array logic) unit mounted on the read-out board. Denoting X_i and Y_i the views of the plane i and P_i the analogic OR ($P_i = P_{i,x} + P_{i,y}$) of the two views x and y of plane i, we have the following main trigger:

$$((X_1 \text{ AND } P_3) \quad \text{AND} \quad (Y_1 \text{ OR } P_2)). \tag{1}$$

The threshold is set at 0.69 keV μm^{-1}. Particles are therefore required to cross the detector in order to have a trigger to read the event. The minimum energy to have a trigger, determined with Monte Carlo simulations, is shown in table 1. The 0.69 keV μm trigger threshold, necessary

to optimize the detector for high-Z nuclei observation (of higher interest for LF), reduces the proton detection efficiency at high energies (above 100–200 MeV). As the energy increases the energy deposited decreases and reduces the trigger probability: above 400 MeV the efficiency is $\simeq 7\%$. Particles from both sides of the detector are read: however, the material crossed is different in the two cases, since particles cross the 0.2 mm Cu window on one side (closer to the cosmonaut's head) and $\simeq 2$ cm of electronics on the other. This requires a correction in the energetic spectrum of low-energy particles coming from this direction, but, aside from nuclear fragmentation in the interposed material, does not appreciably affect the nuclear composition.

Data from the FIFO are then sent, through an interface board, to a PCMCIA digital acquisition board housed in the laptop. The interface board also handles data coming from the cosmonaut joystick and the LEDs used for eye adaptation. The acquisition software includes a data quick-look to be performed by the cosmonaut who can also add personal comments after the conclusion of each session. Data storage is performed on PCMCIA hard disks; data transfer to Earth is performed by the crew who bring the hard disks to Earth when returning from Mir.

3. Data analysis

The study of the radiation environment on-board manned spacecrafts allows evaluation of the dose absorbed by the astronauts in order to assess the risks involved in space missions. The complexity of the information required for a detailed comprehension of the radiation environment grew with the improvement of the detectors and the understanding of the near-Earth and interplanetary radiation environment. The use of active detectors allows a measurement in real time of the nature of charged radiation impinging on the spacecraft and the modifications of the cosmic ray flux due to the interaction with the material of the spacecraft itself. These studies have to be carried forth both in solar-quiet and active conditions, in order to take into account the dose absorbed by astronauts during SPEs. The time and intensity variability of these events make them real threats to long-term activities outside the geomagnetic shielding such as a mission to Mars [17]. In this work we analyse the performance of the silicon detector and report on cosmic ray measurements.

3.1. Calibration

Each acquisition session begins with the calibration of the detector. The position and RMS (root mean squared) of the electronic pedestal of each silicon strip is evaluated with 1024 measurements. Figure 3 shows the histograms of average and RMS values of the detector strips. The thin line refers to one of the first acquisition sessions (14 February 1998), while the thick line refers to one of the last (31 July 1999). Note how the position of the pedestal has remained constant during work. In addition, the noise of the pedestal has decreased (the RMS of seven ADC channels during the first session decreases to four to five channels in the 1999 sessions), proving the stability of the electronics and the absence of measurable detector degradation. Plane 1 has a lower pedestal offset than planes 2 and 3. This results in a double-peaked structure in the average value with lower pedestal values due to plane 1 and higher values to planes 2 and 3. It is also to be noted that noise measurements on-board Mir are lower than those obtained during ground tests, probably due to a more stable power source. After the calibration, which lasts about 3 min, data acquisition begins. For each trigger, data are converted and pedestal suppression is performed, keeping only the information from those strips which show an energy release above 3 RMS from the calculated pedestal.

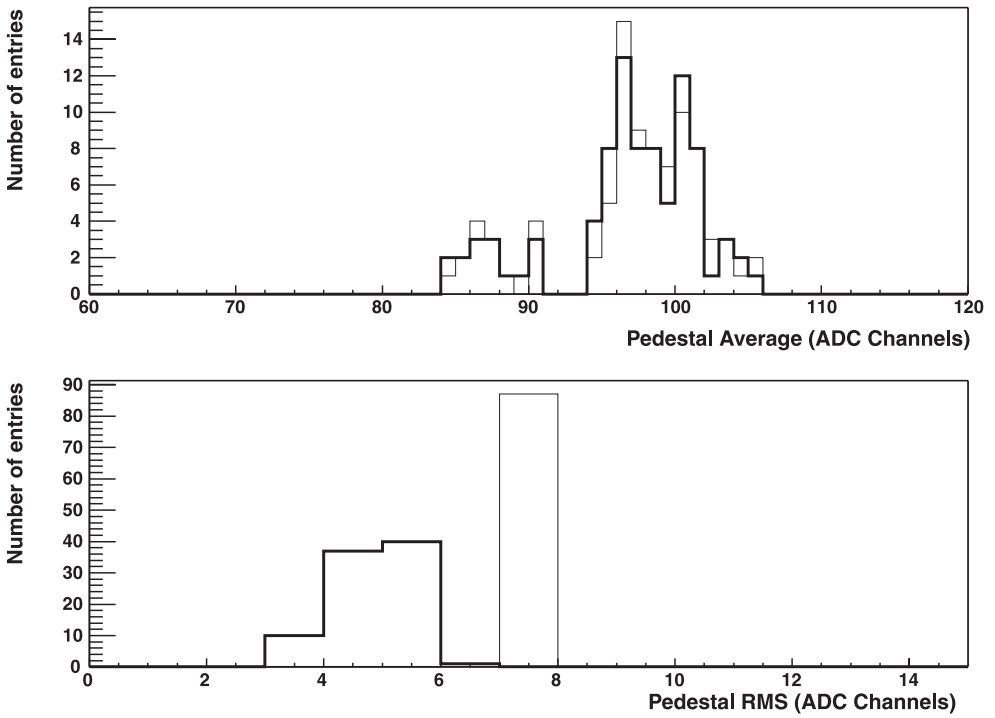

Figure 3. Top, histogram of the average value of the electronic pedestals of each detector strip. The data refers to the sessions of 14 February 1998 (thin line) and 31 July 1999 (thick line). Bottom, histogram of the RMS value of the electronic pedestals for the sessions of 14 February 1998 (thin line) and 31 July 1999 (thick line).

3.2. Detector response and linearity

Particle flux in low Earth orbit basically depends on two parameters: the geomagnetic shielding and solar activity. The former is higher at the geomagnetic equator and thus results in a lower flux. At higher latitudes the shielding is lower and particle flux increases. Another cause of increase is related to SPEs caused by coronal mass ejections or solar flares.

The space station Mir has a 51.6° inclination orbit and an altitude varying between 300 and 400 km. Particle flux on-board Mir varies along the orbit according to the geomagnetic latitude and passage through the South Atlantic Anomaly, where the particle flux increases considerably due to the presence of trapped protons. Figure 4 shows a typical radiation acquisition session with the SilEye-2 detector: a plot of the number of events as a function of time displays oscillatory behaviour typical of the passage between high- and low-latitude regions. The highest peaks are present during passage in the SAA where the particle rate increases by an order of magnitude. The middle curve shows the rate of $Z \leqslant 4$ particles (mostly protons). The lower curve shows the rate of $Z > 4$ nuclei: this component does not increase in the SAA as much as proton and helium. The high-latitude and SAA flux increase is more evident if plotted as a function of position, as shown in figure 5.

The detector response to incoming particles can be divided into two broad categories: below and above $\simeq$100 MeV n^{-1}. In the former case, the energy release increases as the particle crosses the planes. Above $\simeq$100 MeV n^{-1} the energy release can be assumed to be constant with differences due to energy loss fluctuations in each plane. Particles belonging to

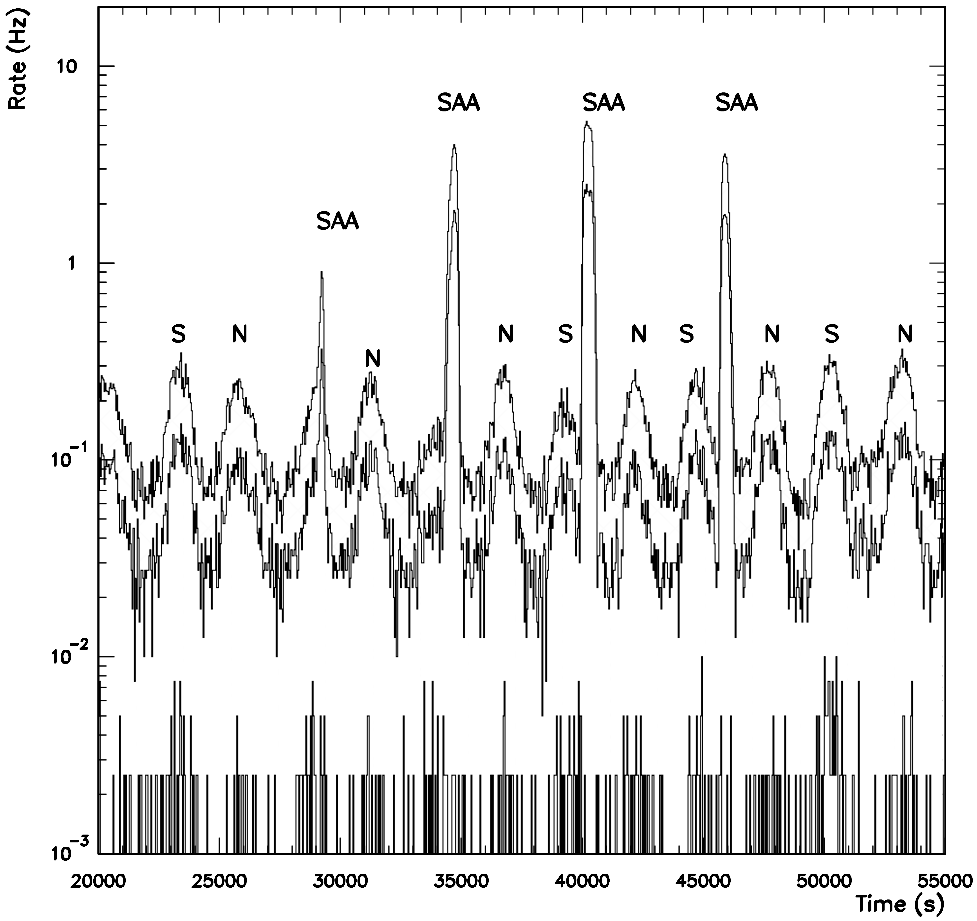

Figure 4. Particle rate as a function of time for a typical acquisition session. Top curve, acquisition rate for all events; centre curve, particle rate of $Z \leqslant 4$, $E > 40$ MeV n^{-1}; bottom curve, particle rate of $Z > 4$, $E > 40$ MeV n^{-1}. The peaks with a rate of about 0.3 Hz correspond to passage through the northern (N) or southern (S) regions; the peaks above 1 Hz correspond to passage through the South Atlantic Anomaly.

this interval can be selected if the energy release between the first and last plane does not differ by more than 20%. The E_{con} column of table 1 shows the threshold energy for different nuclei selected with this cut. The calibration of the device is performed with the aid of Monte Carlo simulations using Geant 3.21 software for the energy loss calculation in the detector for all nuclei involved and cross-checked with SRIM [18], a program devoted specifically for the calculation of ion energy loss in matter. With the additional requirement of selecting single-particle events, nuclei can be identified according to their total energy released in the detector as shown in figure 6. In addition to the large proton and helium contribution (not separated with this approach), abundant nuclear species such as boron, carbon, nitrogen, etc up to iron can be distinguished. The probability distribution of the energy release by a particle in a thin absorber is described by a Landau distribution as a function of the adimensional variable λ:

$$f(\lambda) = \int_0^\infty u^{-u}\, \mathrm{e}^{-u\,\lambda} \sin(\pi u)\, \mathrm{d}u. \tag{2}$$

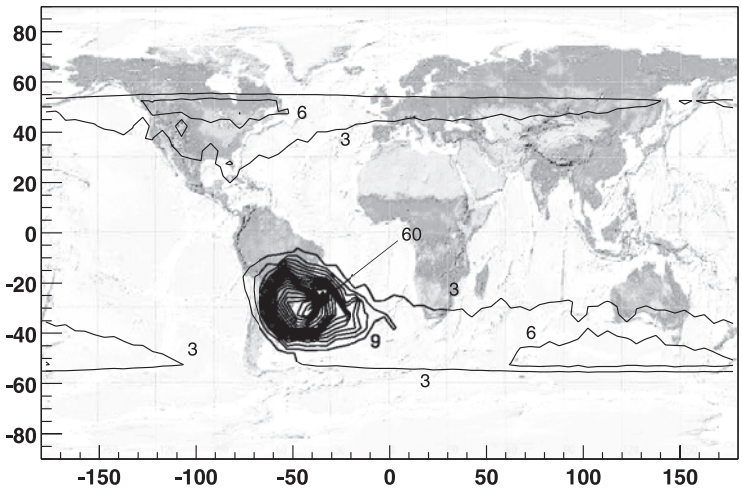

Figure 5. Acquisition rate as a function of position (Y, latitude, degrees; X, longitude, degrees) for all solar quiet sessions. It is possible to see the increase in the SAA region. Each contour level represents a flux increase of 3 Hz.

In order to extract calibration and nuclear abundance information, nuclear peaks have been fitted with a Landau distributions per nucleus. The fit has considered the nuclei from B to Si (10 distributions for 10 nuclei). Each distribution can be characterized by three free parameters P_i according to the following equation:

$$f(\lambda) = P_1 \int_0^\infty u^{-u}\, \mathrm{e}^{-u\,P_2(\lambda - P_3)} \sin(\pi u)\, \mathrm{d}u \tag{3}$$

where P_1 is proportional to the height, P_2 is proportional to the width and P_3 is proportional to the position of each nuclear distribution. The fit uses 32 free parameters: 30 for the 10 Landau distributions and two for an exponential tail used to estimate the $Z < 4$ contamination over B and C. With this approach it is possible to take into account reciprocal contamination of different nuclei; the good agreement of data with the fit, with a normalized $\chi^2 = 3.1$ proves the excellent behaviour of the detector. Subsequently, we performed a linear fit of the values of P_3 (in ADC channels) of each nuclear species, corresponding to the peak of the distributions (the most probable energy release) as a function of the square of the charge of the incident particle. The correlation coefficient of $R = 1$ shows the good detector linearity. A fit of the correlation between the theoretical energy loss (evaluated using Monte Carlo simulations) and the measured ADC values is used to determine the conversion factor of the detector: this is equal to 13.56 channels/MeV, corresponding to an ADC resolution of 74 keV/channel (with $R = 0.9996$).

3.3. Nuclear abundances

From the fit of the Landau curves it is possible to derive the nuclear relative abundances inside Mir in different positions and solar activity conditions. In this case we have considered solar-quiet days in order to provide a reference for subsequent analysis of solar particle events. We have divided the data set according to the McIlwain parameter L and the geomagnetic field B in three regions: galactic cosmic ray region (GCR, $L > 2$), South Atlantic Anomaly (SAA, $L < 2$ and geomagnetic field $B < 0.25$ G), and the remaining region ($L < 2$,

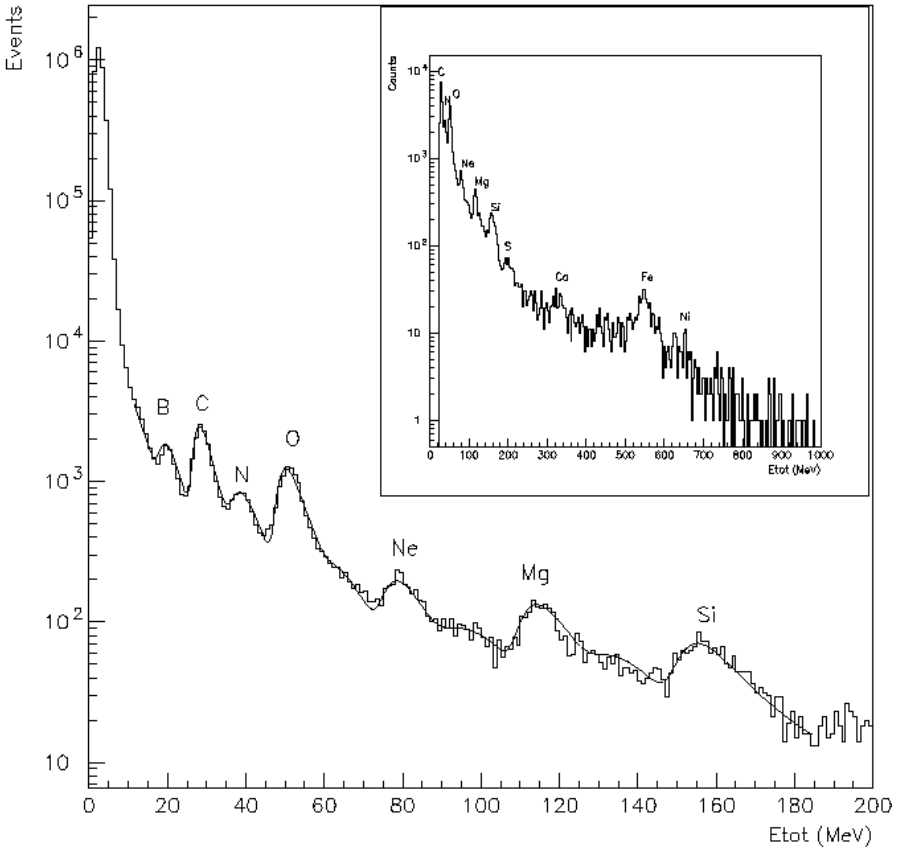

Figure 6. Nuclear identification capabilities of SilEye-2 for nuclei up to Si. In the inset is shown the contribution of nuclei up to Ni. The full curve corresponds to a fit using a sum of 10 Landau distributions, one per nuclear species (see text).

$B \geqslant 0.25$ G). The McIlwain parameter L represents, at a first approximation, the value (expressed in Earth radii) at which the magnetic field line passing through the point considered intersects the geomagnetic equator. In the case of low Earth orbits (such as Mir) values close to $L = 1$ are in proximity to the equator and increase at higher latitudes. For a detailed definition see [6]. This reference system is particularly useful since charged particles spiral along the magnetic field and bounce between the mirror points at values of constant L. In a given point of the orbit, the geomagnetic cut-off C determines the minimum energy for primary cosmic rays to reach Mir and to be detected by SilEye. Note that this value is valid for particles orthogonal to the local field line and outside Mir. In addition, the particle energy inside the station can be modified by the interposed material of the station and the presence of nuclear interactions, so it should be used only as a reference. Particles with energy equal to or lower than the energies shown in the E_{abs} column of table 1 are absorbed by the 3 mm Al material of the external hull of the station. The E_{min} column of table 1 shows the minimum kinetic energy necessary for trigger (after passage through the hull of the Mir). This implies that a 50 MeV n^{-1} carbon nucleus would have the

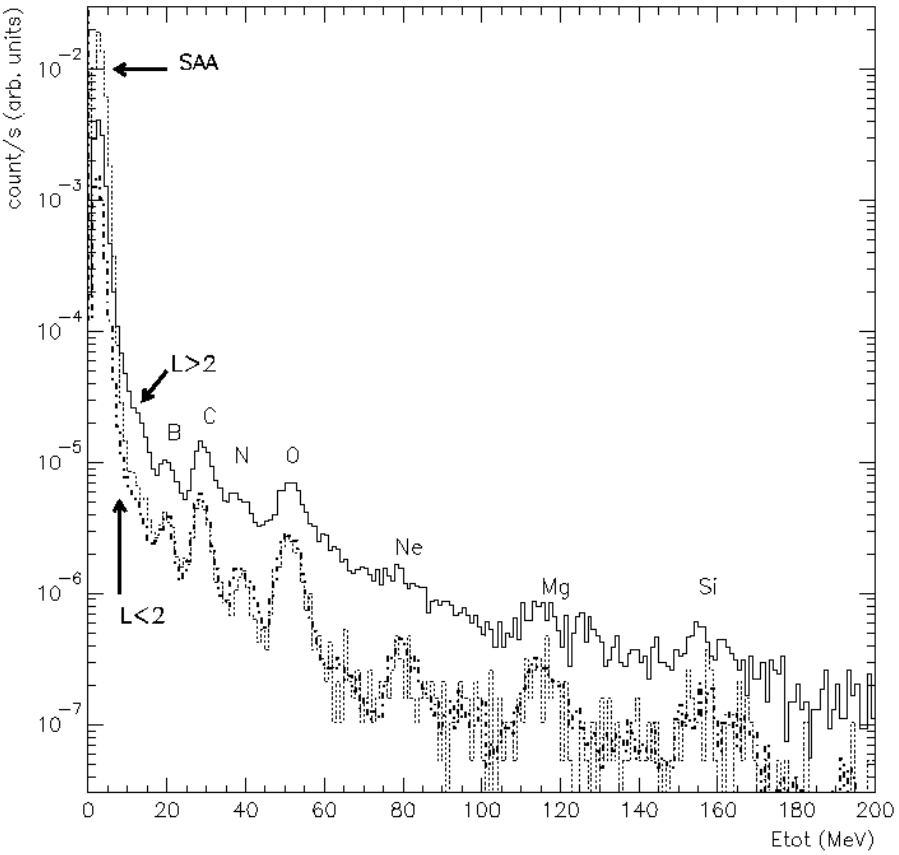

Figure 7. High-energy nuclear abundances: full curve, galactic ($L > 2$) component; dotted curve, SAA component ($L < 2$, $B < 0.25G$); broken curve, remaining region ($L < 2$, $B \geqslant 0.25G$). The SAA region has a higher proton flux due to trapped particles but $Z > 5$ particles are equally abundant to the $L < 2$ region due to the equivalent cut-off. In the case of the galactic component, the lower geomagnetic cut-off results in a higher integral particle flux so that $Z > 5$ nuclei are more abundant.

energy to cross (in orthogonal incidence conditions) the hull of the station but could not give a trigger in the detector: in this experiment the minimum trigger energy for carbon is 90 MeV n^{-1}, of which 20 MeV n^{-1} are lost in the Al of the station. Naturally the 3 mm Al thickness assumed only represents a lower value, since the station and the equipment contained can be interposed between the detector and the local field line along which the particles come.

At $L = 2$, $C = 3.9$ GV while at high latitude ($L = 4.4$) $C = 0.8$ GV. These two values represent the minimum cut-off for a given region; they correspond to a minimum kinetic energy (for a particle with a mass/charge ratio of 2) of $\simeq$150 MeV n^{-1} ($C = 0.8$ GV) and $\simeq$1600 MeV n^{-1} ($C = 3.9$ GV). Particles have been selected with the same cut described in the previous subsection. At these energies particles lose only a small fraction of their kinetic

Table 2. Relative abundances normalized to carbon in the three regions for particle with $E > E_{con}$ (see text).

Z	$L > 2$ ($C > 0.6$ GV)	$L \leqslant 2$ ($C > 3.9$ GV)	SAA ($C > 3.9$ GV)	Cosmic ray 600–1000 MeV n^{-1} [21]
5 (B)	0.63 ± 0.09	0.53 ± 0.35	0.55 ± 0.09	0.307 ± 0.005
6 (C)	1 ± 0.1	1 ± 0.06	1 ± 0.12	1 ± 0.02
7 (N)	0.41 ± 0.06	0.34 ± 0.08	0.22 ± 0.04	0.274 ± 0.007
8 (O)	0.65 ± 0.07	0.66 ± 0.08	0.77 ± 0.17	0.93 ± 0.02
10 (Ne)	0.33 ± 0.06	0.13 ± 0.02	0.12 ± 0.02	0.149 ± 0.004
12 (Mg)	0.07 ± 0.02	0.13 ± 0.02	0.12 ± 0.02	0.187 ± 0.005
14 (Si)	0.05 ± 0.02	0.1 ± 0.02	0.1 ± 0.02	$0.131\,58 \pm 0.000\,03$

Table 3. Integral fluxes measured in the three regions above for particles with $E > E_{con}$ of table 1.

Z	$L > 2$ ($C > 0.6$ GV) part (cm^{-2} sr^{-1} s^{-1})	$L \leqslant 2$ ($C > 3.9$ GV) part (cm^{-2} sr^{-1} s^{-1})	SAA ($C > 3.9$ GV) part (cm^{-2} sr^{-1} s^{-1})
5 (B)	$(6.6 \pm 0.6) \times 10^{-5}$	$(1.6 \pm 1) \times 10^{-5}$	$(1.5 \pm 0.2) \times 10^{-5}$
6 (C)	$(10.5 \pm 0.5) \times 10^{-5}$	$(3.0 \pm 0.1) \times 10^{-5}$	$(2.6 \pm 0.2) \times 10^{-5}$
7 (N)	$(4.3 \pm 0.5) \times 10^{-5}$	$(1.0 \pm 0.2) \times 10^{-5}$	$(0.59 \pm 0.08) \times 10^{-5}$
8 (O)	$(6.8 \pm 0.4) \times 10^{-5}$	$(2.0 \pm 0.2) \times 10^{-5}$	$(2.0 \pm 0.3) \times 10^{-5}$
10 (Ne)	$(3.5 \pm 0.5) \times 10^{-5}$	$(0.38 \pm 0.03) \times 10^{-5}$	$(0.31 \pm 0.06) \times 10^{-5}$
12 (Mg)	$(0.7 \pm 0.2) \times 10^{-5}$	$(0.39 \pm 0.05) \times 10^{-5}$	$(0.33 \pm 0.06) \times 10^{-5}$
14 (Si)	$(0.5 \pm 0.2) \times 10^{-5}$	$(0.29 \pm 0.15) \times 10^{-5}$	$(0.26 \pm 0.05) \times 10^{-5}$

energy in crossing the hull of the station: again, using 3 mm of Al as a reference, we find that, for instance, a 150 (1600) MeV H loses 3.4 (1.3) MeV to enter the station. In the case of other nuclei, the values are similar: if we consider carbon, we have 4.8 (1.2) MeV lost for 150 (1600) MeV n^{-1}. The particle distributions of the three regions are shown in figure 7. The full curve shows the galactic component, which has a higher flux due to the lower geomagnetic cut-off. This allows particles with lower energy to reach Mir and be detected by SilEye resulting in a higher particle count. The wider energy range implies a larger energy release range, resulting in the peaks being less sharply defined. Over this range, the proton and helium flux is lower than that measured in the SAA (dotted curve) where the trapped component is dominant if compared with galactic and $L < 2$ abundances. Indeed, the $L < 2$ curve (broken) has a lower $Z \leqslant 2$ flux if compared with SAA but an equal $Z \geqslant 5$ flux, since in both cases the component selected at this energy is the same. From these distributions it is possible to reconstruct relative abundances and absolute integral fluxes for the different nuclear species (shown, respectively, in tables 2 and 3). Thus absolute fluxes represent an average above the regions where the geomagnetic cut-off is higher than the minimum values of 3.9 and 0.8 GV and can be as high as 16 GV. Determination of the proton spectrum requires detailed corrections for the energy-dependent trigger efficiency so we currently present only $Z > 4$ results (where the trigger efficiency can be assumed to be equal to 1). Table 2 also shows the relative cosmic ray abundances at 1 AU [21] measured in the energy range of $\simeq$1 GeV. It is possible to see how, especially for the $L < 2$ regions, notwithstanding the bulk of Mir, the data are in general in agreement. There are, however, the following notable differences.

- An overabundance of B with respect to C. It is roughly twice the 1 AU value in all three regions. This could be accounted for as secondary production due to hadronic interactions.

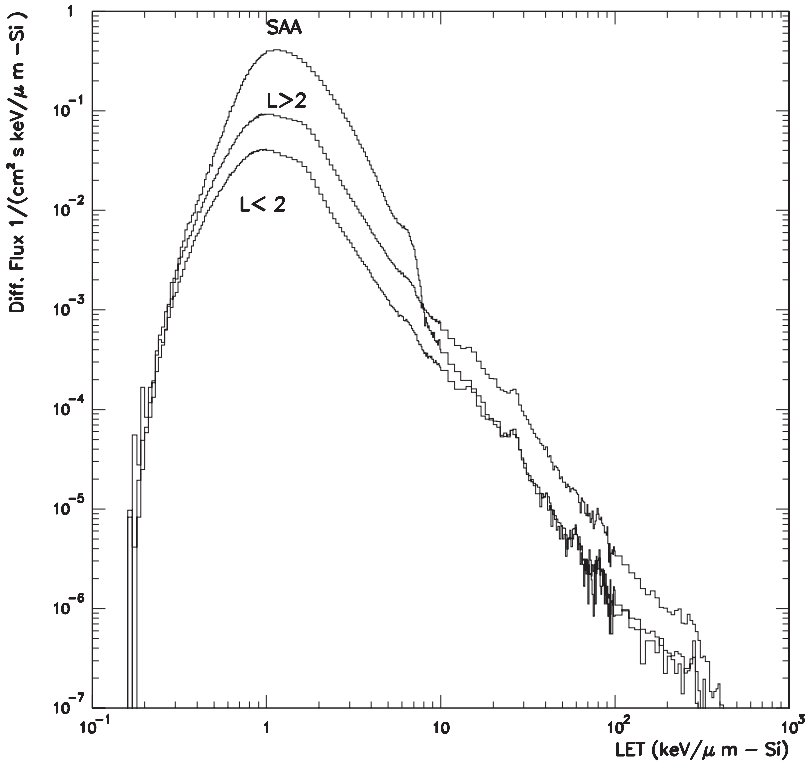

Figure 8. Linear energy transfer in silicon for solar quiet period measured with SilEye-2 (solar quiet sessions between August 1998 and August 1999). Top, SAA region. Centre, galactic ($L > 2$) region. Bottom, remaining region ($L < 2$, outside the SAA.

- A higher amount of N in the $L > 2$ region compared with the other regions and 1 AU data. This could be due to a larger production of secondary N at lower energies.
- A lower amount of oxygen nuclei in $L > 2$ and $L < 2$ regions (the SAA value is in agreement within errors with the 1 AU data). Also in this case the effect can be explained with a higher hadronic interaction cross section for O with respect to C: oxygen could be considered as being composed of four alpha particles (He nuclei) and carbon of three. Thus, if we assume the ratio of the cross sections to be equal to the ratio nucleons of carbon and oxygen ($\frac{12}{16} = 0.75$) and we multiply by the original flux of 0.93 we obtain an abundance of 0.7.
- A higher amount of Ne and a lower amount of Mg and Si in the $L > 2$ region.

In all cases it is clear that a crucial role is being played by hadronic interactions in matter, but an accurate estimate of the processes involved is complicated by the estimation of the energy-dependent cross sections and the amount of material interposed between SilEye and the exterior of the station. Given the conditions of this measure, the agreement with 1 AU data is rather good: the larger differences occur in the $L > 2$ region, where the cut-off is lower and particles have a wider energy range. To improve the measure of cosmic ray abundances inside Mir it will be necessary to separate sessions and incident angles in order to obtain a clearer sample of cosmic rays.

3.4. Linear energy transfer

The LET in silicon measured with SilEye-2 is shown in figure 8: in this work we present solar-quiet period data for the three geomagnetic regions described in the previous section. The LET is obtained by normalizing the total energy release to the angle of incidence for single- and multiple-track events. The topmost curve shows the SAA, where trapped protons are the dominant contribution; the galactic nuclear flux (middle curve) is dominant at LET above 8 keV μm^{-1}. The bottom curve represents LET at $L < 2$ and outside the SAA: the proton component is below the previous two regions, and the high LET component is, as expected, equal to the SAA region. In these two regions the nuclear component is lower than in the $L > 2$ zone due to the higher geomagnetic cut-off. As previously mentioned, trigger efficiency for protons (which constitute the peak at 1 keV μm^{-1}) varies according to the incident energy: a detailed Monte Carlo simulation, currently in progress, is thus required to reconstruct the original proton spectrum, in order to derive, from the measured LET, the dose absorbed by the cosmonauts. The different nuclear abundances and fluxes result in different LETs and therefore different doses absorbed by the astronauts. If we evaluate the dose absorbed in silicon (considering the component above 1 keV μm) from the LET of a typical session (20 October 1998) we obtain 103 ± 10 μGy d^{-1} in the high-latitude region, 271 ± 15 μGy d^{-1} in the SAA and 34 ± 3 μGy d^{-1} in the remaining region. GCR values are lower than those presented in [22] of 146.74 μGy d^{-1} (GCR) and in [9] of 172.8 μGy d^{-1}. However, in the previous experiments the instrument sensitivity extended below the SilEye limit of 1 keV μm. In addition, in [22] a tissue-equivalent proportional counter is used so that the LET in water is measured. In [9] the measurement is made in silicon and the relation $\mathrm{LET}_\infty = 1.193 \times \mathrm{LET}_{\mathrm{silicon}}$ (where LET_∞ is the LET in water) is used. If we consider the SAA, the value presented by [22] is 233.31 μGy d^{-1}, in good agreement with our measurement, although they are lower than the value of 6912 μGy d^{-1} of [9] due to the increased flux of high-energy trapped protons which release less than 1 keV μm^{-1}. In all cases we find in the SAA (as expected) the highest absorbed dose due to the presence of trapped protons. The equivalent dose, however, is at the maximum in the $L > 2$ region where the cut-off is lowest and $Z > 5$ particle flux is higher: the dose equivalent (ICRP-1990) values are 840 ± 50 μSv d^{-1} in the $L > 2$ region, 600 ± 40 μSv d^{-1} in the SAA and 250 ± 20 μSv d^{-1} in the remaining low-latitude region.

4. Conclusions

In this work we have presented the in-flight performance of the SilEye-2 detector and its first observational results. The good behaviour of the detector and its particle identification capabilities enable the study of the cosmic ray and radiation environment and its short- and long-term temporal variations. Analysis is currently in progress to determine relative abundances and fluxes in these conditions and in the presence of solar particle events and to improve the identification capabilities of the device for low-Z nuclei and at lower energies. Linear energy transfer measurements will be as well used to characterize the radiation environment on-board the Mir space station on solar quiet and active days.

Development is planned for a future detector with the construction of two new devices to continue and extend the observational capabilities of SilEye-2 on the International Space Station: Sileye-3/Alteino. This detector, to be launched in 2002, is similar in size (eight wafers each 8×8 cm^2) to Sileye-2 and, in addition to new electronics and detectors, will also carry an electroencephalograph to perform a real-time correlation between

light flash perceptions by astronauts and cosmic rays. The technology developed for SilEye-3 will be used in the construction of a larger facility, originally proposed in [19] and evolved in the Altea (SilEye-4) project [20], currently under development.

References

[1] Selesnick R S, Cummings A C, Cummings J R, Mewaldt R A, Stone E C and von Rosenvinge T T 1995 *J. Geophys. Res.* **100** 9503
[2] Tobias C A 1952 *J. Aviat. Med.* **23** 345
[3] D'arcy F J and Parker N A 1962 *Nature* **196** 1013
[4] Malachowski M J 1978 *LBL Report* LBL-5683 National Technical Information Service, Springfield, VA
[5] Horneck G 1992 *Nucl. Tracks Radiat. Meas.* **20** 185
[6] McIlwain C E 1961 *J. Geophys. Res.* **66** 3681
[7] McNulty P J 1996 *IEEE Trans. Nucl. Sci.* **43** 475
[8] Reitz G *et al* 1996 *Radiat. Meas.* **26** 679
[9] Sakaguchi T *et al* 1999 *Nucl. Instrum. Methods* A **437** 75
[10] Galper A *et al* 1996 *Proc. 6th Eur. Symp. on Life Sciences Research in Space (Trondheim)*
[11] Morselli A *et al* 1997 *Proc. 25th Int. Conf. RC (Durban)* OG 10.2.8 vol 5, p 45
[12] Bidoli V *et al* 1997 *Nucl. Instrum. Methods* A **399** 477
[13] Bidoli V *et al* 2000 *Adv. Space Res.* **10** 2075
[14] Avdeev S *et al* 2001 *Acta Astronaut.* submitted
[15] Bidoli V *et al* 2001 *Astrophys. J. Suppl.* **132 2** 365
[16] Sparvoli R *et al* 2000 *Nucl. Phys.* B (*Proc. Suppl.*) **85** 28
[17] Spillantini P 2000 *Nucl. Phys.* B (*Proc. Suppl.*) **85** 3
[18] Ziegler J F 1985 *The Stopping and Range of Ions in Solids* (Oxford: Pergamon)
[19] Casolino M *et al* 1997 *Nuovo Cimento* D **19** 10
[20] Bidoli V *et al* 1999 ESA SP-433
[21] Simpson J A 1983 *Ann. Rev. Nucl. Part. Sci.* **33** 323
[22] Badhwar D and Cucinotta F A 1998 *Rad. Res.* **149** 209